Performance study and conceptual design for the first implementation of AGATA at the in-flight RIB facility of GSI

C. Domingo-Pardo[a,b], D. Bazzacco[c], P. Doornenbal[d], E. Farnea[c], A. Gadea[a], J. Gerl[b], H.J. Wollersheim[b]
The AGATA Collaboration

[a] *IFIC, CSIC-University of Valencia, Valencia, Spain*

[b] *GSI Helmholtzzentrum für Schwerionenforschung GmbH, Darmstadt, Germany*

[c] *Istituto Nazionale di Fisica Nucleare, Sezione di Padova, Italy*

[d] *RIKEN, Japan*

Abstract

The main objective of the Advanced GAmma Tracking Array (AGATA) is the investigation of the structure of exotic nuclei at the new generation of RIB facilities. As part of the preparatory phase for FAIR-NUSTAR, AGATA is going to be installed at the FRS fragmentation facility of the GSI center for an experimental campaign to be performed in 2012 and 2013. Owing to its γ-ray tracking capabilities and the envisaged enhancement in resolving power, a series of in-flight γ-ray spectroscopy experiments are being planned. The present work describes the conceptual design of this first implementation of AGATA at GSI-FRS, and provides information on the expected performance figures. According to the characteristics of each particular experiment, it is foreseen that the target-array distance is adjusted in order to achieve the optimum compromise between detection efficiency and energy resolution, or to cover an specific angular range of the emitted electromagnetic radiation. Thus, a comprehensive Monte Carlo study of the detection sensitivity in terms of photopeak efficiency, resolution and peak to total ratio, as a function of the target-array distance is presented. Several geometry options have been investigated, and MC-calculations indicate that a remarkable enhancement in resolving power can be achieved when double-cluster AGATA detectors are developed and implemented. Several experimental effects are also investigated. This concerns the impact of passive materials between the target and the array, the angular distribution of the detection efficiency and the influence of target thickness effects and transition lifetimes in the attainable detection sensitivity. A short overview on halflife measurements via lineshape effects utilizing AGATA is also presented.

Key words: gamma-ray spectroscopy, tracking, Monte Carlo

1. Introduction

The study of nuclear structure far-off stability benefits from advances in both, acceleration techniques, as well as in detection systems. Since their invention in 1960, semiconductor germanium detectors represent a key instrument in the field of high-resolution γ-ray spectroscopy. Since then, the unsurpassed energy resolution of germanium detectors has led to the discovery of new features and astounding properties of the atomic nucleus. Developments such as Ge-arrays like EUROBALL [1] and GAMMASPHERE [2] led to about two orders of magnitude improvement in resolving power when compared to the first generation of Compton-suppression arrays like HERA [3] or TESSA3 [4]. Remarkable results were, for example, the measurement of superdeformed nuclei with very high-angular-momentum states [5, 6, 7, 8], thus revealing nuclear rotating systems with moments of inertia larger than 80 $\hbar^2 MeV^{-1}$.

At present, the hot topics of nuclear structure with Radioactive Ion Beams (RIBs) concern the evolution of shell gaps and the related changes in magic numbers far-off stability; breakdown of isospin symmetry and its interplay with nuclear shape evolution and shape coexistence phenomena; determination of the drip-line border of the nuclei chart and its link to open quantum systems, that in turn allow for understanding the coupling between bound states and the continuum; collectivity phenomena and electric and magnetic strength in nuclei, including also the investigation of giant resonances, as well as substructures in the Pygmy Dipole Resonance [9]. A deeper understanding of these scientific themes will become possible in the next future thanks to the combination of more exotic RIBs with state-of-the-art γ-ray detection systems. The latter concern the concept of γ-ray tracking. Owing to this novel approach, new generation arrays of 2D-segmented 3D-position sensitive detectors, such as the Advanced GAmma Tracking Array (AGATA) in Europe [10] and the Gamma-Ray Energy Tracking Array (GRETA) in the USA [11] are being developed and early implementations are already used for in-beam γ-ray spectroscopy experiments.

After undergoing a research and development phase including Monte-Carlo simulations and design studies [12, 13, 14, 15, 16, 17, 18], detector characterization [19, 20, 21, 22, 23,

24, 25, 26], technical developments [27, 28, 29], as well as a commissioning and in-beam test of the system [30, 31, 32, 33, 34, 35, 36, 37, 38] a sub-array of AGATA, the so called AGATA Demonstrator, has been successfully set-up in operation at the stable ion beam facility of Laboratori Nazionali di Legnaro LNL-INFN (Italy).

In order to exploit best the complementarity offered by the different facilities in Europe, AGATA has been conceived as a peripatetic apparatus, which will itinerate from one facility to another. Thus, the next experimental campaign will be carried out, during 2012 and 2013, at the GSI center for heavy ion research (Germany) in the framework of PreSPEC [39], which represents the preparatory phase for HISPEC/DESPEC at FAIR. HISPEC and DESPEC, which stand respectively for High-Resolution In-flight SPECtroscopy and DEcay SPECtroscopy experiments, will be part of the NUSTAR (NUclear STructure, Astrophysics and Reactions) collaboration. FAIR-NUSTAR will be the major next generation in-flight RIB facility in Europe. Similarly to the existing site at GSI, FAIR-NUSTAR will be based on the production of fragments from GeV/u beams and their separation in the Super-FRS [40]. The forthcoming stay of AGATA at GSI-FRS will benefit already from improvements in the beam intensities, which are a consequence of present accelerator developments towards FAIR. However, there are a number of relevant differences in the experimental conditions of GSI-FRS when compared to the previous host, LNL-INFN, which need to be properly taken into account. Such differences concern mainly the relativistic momentum (typically $\beta \sim 0.43$) and the spatial distribution (FWHM$_X$ $\sim$ 6 cm) of the RIB at GSI-FRS, when compared to the narrow (FWHM$_X$ $\sim$ 2 mm) stable beams, commonly used at LNL-INFN at lower velocities ($\beta \lesssim 0.1$). Thus, in order to optimize its γ-ray efficiency and high intrinsic energy- and spatial-resolution, the configuration of the AGATA detectors needs to be designed according to the characteristics of the ion beam at the final focal plane of the GSI fragment separator (FRS). To achieve this aim, systematic Monte-Carlo (MC) simulations have been performed and their results are reported in this article. Sec. 2 summarizes the general features of the fragmentation facility at GSI, and the typical experimental conditions for in-flight γ-ray spectroscopy experiments using relativistic beams, with particular emphasis on the main differences in the experimental conditions with respect to the previous AGATA campaign, hosted at LNL-INFN.

MC-simulations reported in Sec. 3 illustrate the need of developing new double cluster detectors for an optimal use of AGATA with the RIBs available at GSI-FRS, as well as for HISPEC experiments in the future FAIR-NUSTAR facility. Section 4 shows the attainable γ-ray detection sensitivity for such hybrid AGATA-shell geometries, with a variable number of double- and triple-cluster detectors. This seems convenient because of the non proportionality between efficiency and number of capsules. Also, results reported in that section should allow one to pick-up expected efficiency, resolution and peak to total (P/T) ratios, according to the number of crystals available for the array at the time of each particular experiment. The performance of several combinations of double- and triple-cluster detectors, from 10 up to 40 capsules is displayed and tabulated. Photopeak efficiency, energy resolution and P/T ratios are represented as a function of the distance target-array, which can be adjusted for each particular experiment in order to find the best compromise according to the characteristics of the measurement.

The detection efficiency of AGATA varies with the γ-ray energy, which is also affected by the Lorentz boost. This dependency is reported in Sec. 5 for γ-quanta in the energy range from 500 keV up to 5 MeV and for several AGATA configurations. The Lorentz boost of the relativistic RIBs commonly used at GSI-FRS determines also, to a large extent, the angular distribution of the γ-ray detection efficiency. This relationship becomes of particular interest for a number of experiments (see e.g. [41]), as well as for the determination of reduced transition probabilities of excited states (see Sec. 9). Thus, Sec. 6 shows the angular variation of the photopeak efficiency for two AGATA configurations and for several target-array distances.

In the past campaigns with EUROBALL cluster detectors at GSI-FRS a thin shielding made of lead was commonly utilized for reducing atomic backgrounds. The impact of such additional passive materials on the detection efficiency of AGATA is presented in Sec. 7.

The impact of the halflife of the nuclear transition in combination with target thickness effects is reported in Sec. 8. A short overview on halflife measurement via lineshape effects is described in Sec. 9. Finally, Sec. 10 summarizes the main results and conclusions of the present work.

2. The GSI fragmentation facility and experimental conditions

The production of RIBs at the GSI-FRS facility starts with a high intensity stable beam delivered by the UNILAC linear accelerator, and accelerated to relativistic energies by the SIS18 synchrotron. This primary beam impinges on a target at a high energy, typically between 400 MeV/u and 1 GeV/u. This way, a broad spectrum of radioactive species is produced by means of fragmentation or Coulomb induced fission reactions. The production target is in most cases a Be- or a Pb-layer with a thickness between 2 and 4 g/cm^2. The fragments of interest are selected and transmitted through the fragment separator (FRS) using the Bρ-ΔE-Bρ method. Details on the FRS can be found in Ref. [42]. The spatial profile of the fragments beam at the final focal plane of the FRS depends on several parameters, such as the beam energy and achromaticity. For energies of 100 MeV/u the beam shows a width of $\lesssim$6 cm FWHM in the dispersive horizontal plane X and about 4 cm FWHM on the vertical axis Y (see Fig. 1).

A secondary target, typically with a size of 62.5×62.5 mm^2, is placed at the final FRS focal plane for inducing the reactions of interest in the impinging RIB. The target material is usually gold or lead for Coulomb excitation and beryllium for secondary fragmentation or particle knockout reactions. Thanks to the high secondary beam energy (~100 MeV/u) rather thick targets of 200 mg/cm^2 to 500 mg/cm^2 can be used, which allow one to enhance the reaction rate, while keeping the angular

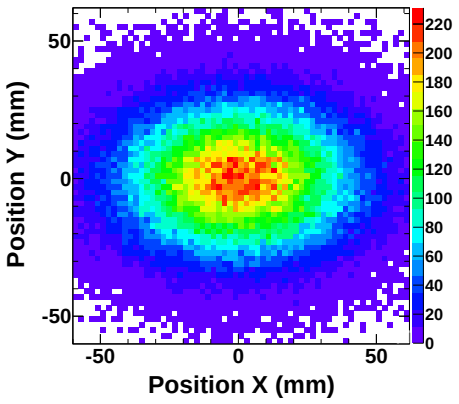

Figure 1: Transversal spatial distribution of the RIB at the final FRS focal plane for an energy of ~100 MeV/u.

straggling of the reaction products within reasonable values of 5-10 mrad. For many cases, such an enhancement on the reaction yield becomes of pivotal importance in order to access very exotic species, which are produced only in very small amounts.

Because of the high ejectile velocity β the measured γ-ray energy E_γ appears shifted with respect to the γ-quantum energy at rest $E_{\gamma,\circ}$. This effect can be corrected by applying the Doppler formula,

$$E_{\gamma,\circ} = E_\gamma \frac{1-\beta cos\theta_\gamma}{\sqrt{1-\beta^2}}, \quad (1)$$

where θ_γ is the angle between the emitted γ-ray and the trajectory of the fragment in the laboratory frame. Thus, the accuracy with which the original γ-ray energy can be determined is challenged by the incertitude in the determination of the angle θ_γ and the velocity at deexcitation time β. In theory, three positions are needed in order to derive the value of the angle θ_γ: the position of the ejectile both at deexcitation time and downstream from the target, and the location of the first γ-ray hit in AGATA. In practice, however, the ion position at deexcitation time can be measured only in an approximate way. Indeed, the two transversal (x, y) coordinates of the fragment are determined, approximately at decay time, utilizing a double-sided silicon-strip detector (DSSD) placed close to the secondary target. At present, there is no technique to measure the z-position of the reaction product at deexcitation time and, particularly for long deexcitation halflifes, this uncertainty dominates the width of the Doppler corrected γ-ray spectrum (see Sec. 8). The location of the reaction products downstream from the target is made by means of the Lund-York-Cologne CAlorimeter (LYCCA) [43], which also enables the measurement of the velocity of the fragments after the target β_{at}. Note that, in general, due to the energy loss in the target this quantity can be smaller than the velocity at deexcitation time β, i.e. $\beta_{at} \leq \beta$, an effect which also has an impact in the attainable resolution (see Sec. 8). Finally, the 3D position sensitivity of AGATA provides the last information needed for the Doppler reconstruction of the γ-ray spectra.

Further details about γ-ray spectroscopy experiments with RIB at GSI-FRS using the RISING array of EUROBALL cluster detectors can be found in Ref. [44].

3. Reference case for the conceptual design The AGATA double cluster detectors

A simplified, although representative, physics case has been simulated in order to evaluate several possible geometrical detector configurations and determine the array design best suited for experiments at GSI-FRS. The figure of performance is based on the attainable γ-ray photopeak efficiency, peak to total (P/T) ratio and energy resolution. The MC-code used for this purpose is the one described in Ref. [15], with minor modifications in order to include the specific spatial x, y-profile of the RIB at the final focus of the FRS (see Fig. 1). Also the event generator of Ref. [15] was used to emit γ-rays with an energy at rest of $E_{\gamma,\circ}$ =1 MeV emitted from a nucleus at a velocity of β = 0.43, equivalent to ~100 MeV/u commonly used for Coulomb excitation and particle knockout experiments at GSI-FRS.

It is worth emphasizing that, for this conceptual design study, the effects of the target thickness and the halflife of the nuclear transition have been explicitly left aside. Such simplifications are convenient in order to tackle the problem in a systematic way. A negligible target thickness ensures no energy loss across the target, which implies a well defined velocity at deexcitation time (β = 0.43). The impact of the target details, such as thickness and composition, in the Doppler reconstructed spectra is reported latter in detail in Sec. 8. A negligible target thickness, in combination with a prompt deexcitation (halflife $t_{1/2}$ = 0) ensures also a well defined emission angle θ_γ. The interplay between the value of the halflife and the target thickness is reported latter in Sec. 9. These effects are expected to influence the performance of the array in the same direction for all configurations and therefore, such assumptions are not expected to affect the conclusions of this section.

Another simplification concerns the γ-ray multiplicity, which has been assumed to be M_γ=1 in all cases. Apart from the atomic background radiation, M_γ=1 is a reasonable assumption for both Coulomb excitation experiments M_γ^{Coulex}=1-2 and particle knockout reactions $M_\gamma^{Knockout}$=3-4.

In order to set-up a versatile γ-ray detection system with a limited number of capsules available, it is foreseen that the distance target-array is adjusted according to the characteristics of each particular experiment. Thus, large (short) target-array distances can be set-up in order to optimize detection resolution (efficiency). This feature is reasonable when the array consists of a relatively small amount of 30-40 capsules. A larger number of detectors covering a solid angle of 2π or more would show approximately a constant variation of the efficiency with the target-array distance. An intermediate distance can be also chosen in order to settle a compromise between efficiency and resolution. The so-called "large" distance corresponds to 23.5 cm, which represents the center of the spherical shell defined by the front surface of the AGATA capsules. The "short" distance

corresponds to a displacement of the target by 150 mm downstream, which means a target-array distance of 8.5 cm. Thus, each simulated geometry case is based on MC-calculations for 6 different target-array distances of 23.5, 18.5, 15.5, 13.5, 11.5 and 8.5 cm. Each simulation contains $5{\times}10^5$ MC-histories, which yields a negligible statistical uncertainty for all quoted results.

γ-Ray tracking is implemented for the reconstruction of the simulated events by applying the MGT-code [45]. This algorithm is used with both packing and smearing distances equal to 5 mm and intrinsic energy resolution for HPGe of 1.9 keV FWHM at E_γ = 1.33 MeV with a noise component of 1 keV.

The first aspect to be considered for the installation of AGATA at GSI is related to constraints arising from the size of the RIB at the final focal plane of the FRS. Such statement also holds concerning future implementations of AGATA for HISPEC experiments at FAIR-NUSTAR. On one hand, as shown in Fig. 1, because of the spatial spread of the RIB a beam-pipe with a diameter of $\gtrsim$80 mm is required in order to avoid excessive interactions of the outgoing reaction products with the beam-pipe itself and another structural materials. Calculations of the ion-beam optics through the current design of the Super-FRS [46] indicate that the size of the beam at its final focal plane should be comparable to the one shown in Fig. 1. On the other hand, the geometrical design of AGATA is done aiming to maximize the solid angle coverage, thus reducing to the minimum the size of the pentagonal holes [15]. The latter turn out to be sufficiently large for the beam output at LNL-INFN, but they are too small for the beam at GSI-FRS. The most straightforward solution would consist of removing two of the central triple clusters of the 1π AGATA configuration, and rotate slightly the array around the vertical axis, as it is shown in Fig. 2-top. Nevertheless, this option shows two strong drawbacks. First, it breaks the symmetry of the array, thus making difficult the distribution of the detectors and lending to an irregular growth and solid angle coverage of the array. Second, the irregular and relatively large insensitive area at forward angles turn out to be the most relevant region in terms of efficiency due to the effect of the Lorentz boost.

One possibility to improve this situation consists of developing and implementing double cluster detectors, which are built of type B and C capsules. This way, the removal of the five capsules of A type positioned around the pentagonal hole in the beam axis is done by implementing an inner ring of five double cluster detectors. Thus, this AGATA implementation will be an hybrid configuration of double and triple cluster detectors, still in a 1π symmetric AGATA configuration (see Fig. 2-bottom). This allows for a large solid angle coverage at forward angles, while leaving enough space for the RIB passing downstream towards LYCCA. Such approach yields a remarkable enhancement in performance when compared with any other possibility based only on triple cluster detectors. This statement is demonstrated in Fig. 3, where the photopeak efficiency, energy resolution and P/T ratio are shown as a function of the distance between the secondary target and the AGATA array. In this case, the geometry based on triple clusters consists of 13 ATCs (39 capsules), as shown in Fig. 2-top. The new hybrid geometry is based on an outer ring of 10 ATCs, supplemented with an inner ring of 5 AGATA Double Cluster (ADC) detectors (40 capsules), as shown in Fig. 2-bottom. Thus, an enhancement of up to 20% in efficiency can be achieved (in relative terms), whereas the resolution and P/T ratios remain essentially the same. The tracking efficiency of MGT typically varies between 60% and 80% for short (8.5 cm) and large (23.5 cm) target-array distances, respectively.

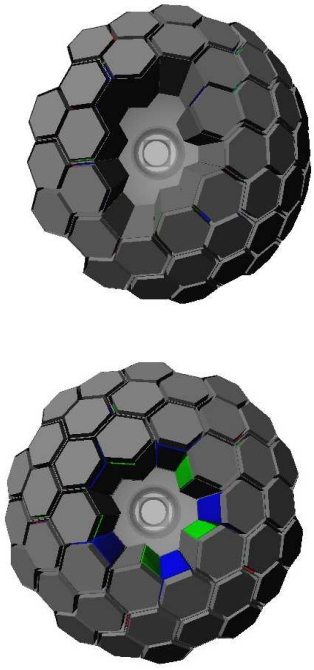

Figure 2: (Top) Shell geometry with 13 triple cluster detectors. (Bottom) Hybrid shell geometry with 5 double- and 10-triple cluster detectors.

The increasing detection sensitivity with decreasing target-array distances reflects both, the effect of the larger solid-angle and the Lorentz boost at velocities of $\beta \sim 0.43$. The latter represents indeed an advantage in terms of detection efficiency, as it is illustrated in the top panel of Fig. 4, where the performance of the 10 T+5 D geometry is shown for a projectile velocity of $\beta = 0.43$ and at rest $\beta = 0$.

Another geometry approaches thoroughly investigated were based on compact cylindrical geometries, where the AGATA triple-cluster detectors were separated from each other, and arranged in a large solid-angle configuration around the target chamber. This approach had the disadvantage that γ-ray tracking could be only effectively applied within each triple-cluster detector, thus reducing the overall performance of the array, and limiting notably the scalability of the array on a long term basis.

In summary, the MC performance figures indicate that an hybrid shell-geometry, based on an inner ring of 5 double cluster detectors, and an outer ring of triple cluster detectors (as many as available) represents the best approach for nuclear structure studies using relativistic RIBs at the GSI-FRS facility and at the future FAIR-NUSTAR site.

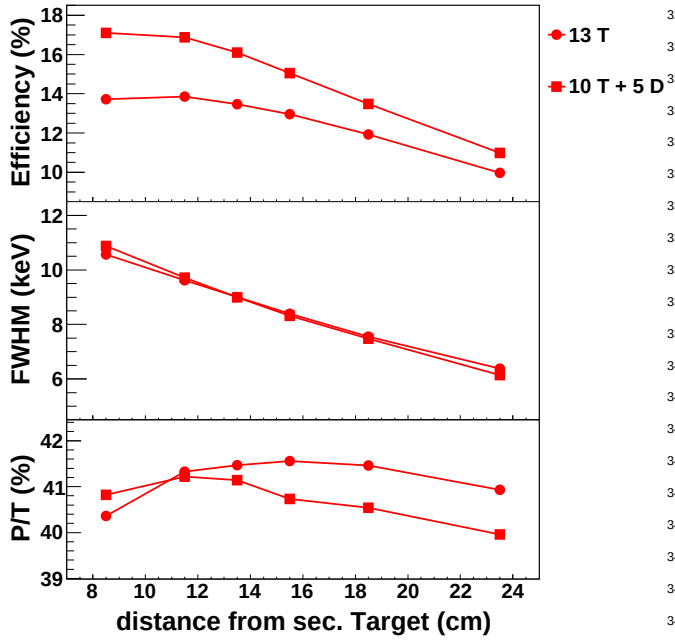

Figure 3: Photopeak efficiency (top) resolution (middle) and P/T ratio (bottom) for two AGATA configurations: 13 triple clusters (circles) and 5 double- plus 10 triple-cluster detectors (squares).

4. Performance of the hybrid shell geometry

Because of the aforementioned non-proportionality between efficiency and the number of capsules present in the array it is worth to quantify the performance of the hybrid array as a function of the number of double- and triple-cluster detectors. Using the reference case described in the section above, table 1 shows the expected performance in terms of γ-ray photopeak efficiency, resolution and P/T-ratio as a function of the number of triple and double cluster detectors available and for several distances from the secondary target to the array. For the sake of clarity, these values are shown in Fig. 5 only for configurations consisting of n triple- and 5 double-cluster detectors (n T+5 D), with $n = 0, 1, \ldots, 10$. Fig. 6 shows the performance for 5 ATC and a variable number of ADCs (5 T+n D), with $n = 0, 1, \ldots, 5$. In the latter figure, also the combination 0 T+5 D is shown. It is worth emphasizing the similarity in performance between the 0 T+5 D and the 5 T+0 D cases (see solid circles and open squares in Fig. 6), which illustrates, once more, the relevance of developing AGATA double cluster detectors for experiments at GSI. Indeed, 10 capsules arranged in a ring of 5 ADCs, show already the same performance as 15 capsules arranged in a half-ring of 5 ATC detectors. In this respect, it is also important to remark the non-linear dependence of the detection efficiency on the number of capsules, which is a consequence of γ-ray tracking. For example, the 5 T+0 D case corresponds to an intrinsic photopeak efficiency of 0.13% per capsule. On the other hand, the 5 T+5 D configuration shows an efficiency of 0.22% per capsule, which indicates a relative enhancement of the detection efficiency per capsule of 66%.

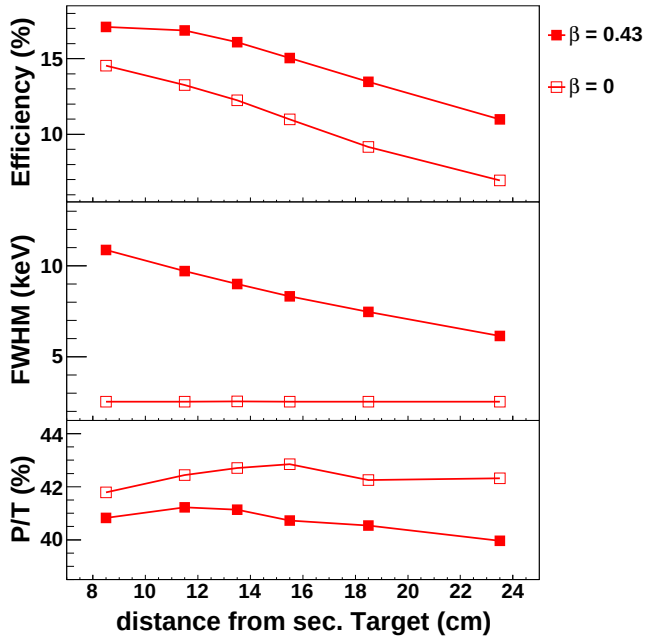

Figure 4: Photopeak efficiency (top) resolution (middle) and P/T ratio (bottom) for the 10 ATC + 5 ADC AGATA configuration, at relativistic projectile energy $\beta = 0.43$ (solid symbols) and at rest (open symbols).

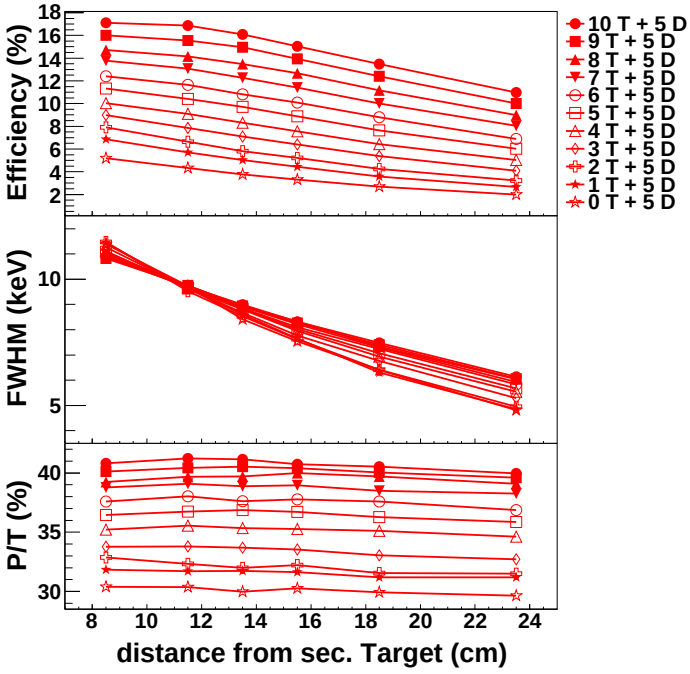

Figure 5: Reference case. Efficiency (top), resolution (middle) and P/T ratio (bottom) as a function of the number of triple (#T) cluster detectors in the setup. The number of double cluster detectors is always 5.

Table 1: Reference case. Performance of the AGATA array as a function of the number of double and triple AGATA cluster detectors. For each configuration indicated in the left-hand side of the table, the three rows represent the efficiency, resolution and P/T ratio, respectively.

# T	# D	distance target-array (cm) 23.5	18.5	15.5	13.5	11.5	8.5	
10	5	11.0	13.5	15.1	16.1	16.9	17.1	ε_γ (%)
		6.1	7.5	8.3	9.0	9.7	10.9	FWHM (keV)
		40.0	40.5	40.7	41.1	41.2	40.8	P/T (%)
9	5	10.0	12.4	13.9	14.9	15.6	16.0	ε_γ (%)
		6.1	7.4	8.3	8.9	9.7	10.8	FWHM (keV)
		39.6	40.0	40.4	40.5	40.4	40.1	P/T (%)
8	5	9.0	11.2	12.7	13.5	14.1	14.7	ε_γ (%)
		6.0	7.3	8.3	8.9	9.7	10.9	FWHM (keV)
		39.1	39.7	40.0	39.7	39.7	39.2	P/T (%)
7	5	8.0	10.0	11.4	12.3	13.1	13.8	ε_γ (%)
		5.9	7.3	8.2	8.9	9.8	11.0	FWHM (keV)
		38.3	38.5	39.0	38.9	39.1	38.8	P/T (%)
6	5	6.9	8.8	10.1	10.8	11.6	12.4	ε_γ (%)
		5.8	7.2	8.1	8.8	9.7	11.1	FWHM (keV)
		36.9	37.6	37.8	37.6	38.0	37.6	P/T (%)
5	5	6.0	7.6	8.9	9.7	10.4	11.3	ε_γ (%)
		5.7	7.1	8.0	8.8	9.7	11.1	FWHM (keV)
		35.8	36.3	36.7	36.9	36.7	36.5	P/T (%)
4	5	5.0	6.4	7.6	8.3	9.1	10.0	ε_γ (%)
		5.5	6.9	7.9	8.8	9.6	11.1	FWHM (keV)
		34.6	35.1	35.3	35.3	35.5	35.2	P/T (%)
3	5	4.1	5.4	6.4	7.1	7.9	9.0	ε_γ (%)
		5.3	6.8	7.8	8.7	9.6	11.3	FWHM (keV)
		32.7	33.0	33.5	33.7	33.8	33.8	P/T (%)
2	5	3.2	4.2	5.2	5.8	6.7	7.9	ε_γ (%)
		4.9	6.4	7.6	8.5	9.5	11.5	FWHM (keV)
		31.5	31.5	32.2	32.0	32.3	32.9	P/T (%)
1	5	2.7	3.6	4.4	5.0	5.7	6.8	ε_γ (%)
		4.9	6.3	7.6	8.6	9.6	11.4	FWHM (keV)
		31.2	31.2	31.6	31.7	31.7	31.8	P/T (%)
0	5	2.0	2.7	3.3	3.8	4.3	5.2	ε_γ (%)
		4.8	6.4	7.5	8.4	9.7	11.4	FWHM (keV)
		29.6	29.9	30.3	30.0	30.4	30.4	P/T (%)
5	4	5.1	6.5	7.6	8.3	9.0	10.1	ε_γ (%)
		5.6	6.9	8.0	8.8	9.7	11.3	FWHM (keV)
		34.7	35.1	35.5	35.4	35.3	35.3	P/T (%)
5	3	4.1	5.3	6.3	7.1	7.8	9.0	ε_γ (%)
		5.3	6.7	7.8	8.7	9.6	11.2	FWHM (keV)
		32.4	33.0	33.4	33.5	33.5	33.8	P/T (%)
5	2	3.2	4.3	5.2	5.9	6.6	7.9	ε_γ (%)
		4.9	6.4	7.7	8.5	9.7	11.4	FWHM (keV)
		31.1	31.6	32.3	32.3	32.5	32.7	P/T (%)
5	1	2.6	3.6	4.4	5.1	5.7	6.8	ε_γ (%)
		4.8	6.2	7.5	8.5	9.5	11.5	FWHM (keV)
		30.9	30.9	31.7	31.9	31.5	32.1	P/T (%)
5	0	2.0	2.7	3.3	3.8	4.3	5.1	ε_γ (%)
		4.7	6.3	7.6	8.4	9.5	11.6	FWHM (keV)
		29.7	30.0	30.2	30.2	30.2	30.2	P/T (%)

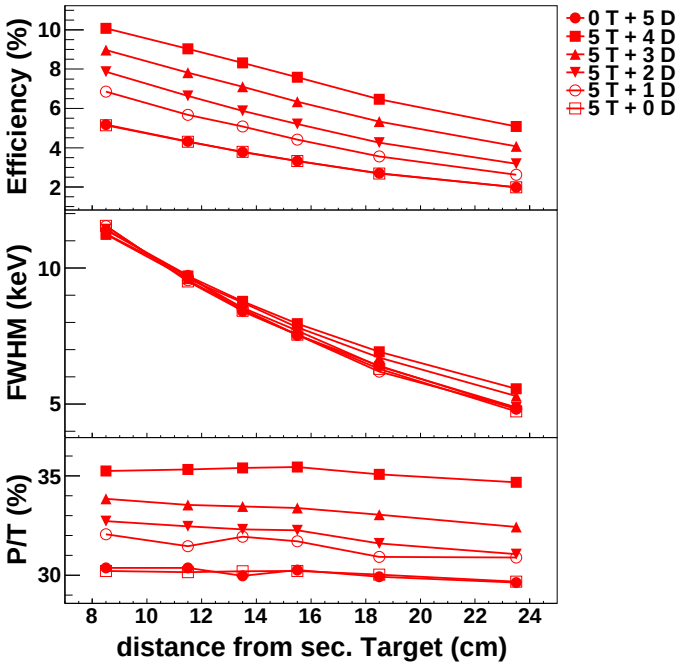

Figure 6: Reference case. Efficiency (top), resolution (middle) and P/T ratio (bottom) as a function of the number of double (#D) AGATA cluster detectors in the setup. All configurations comprise 5 ATC.

By the time of the first experiments with AGATA at GSI, it is expected that at least 5 ATC and 5 ADC become available. This means that for nuclear transitions of 1 MeV emitted at $\beta = 0.43$, photopeak efficiencies in the range of 6 to 11% and energy resolutions of 6 to 11 keV should be attainable (depending on the distance target array) with a P/T ratio of about 36%. Depending on the rate of detector delivery and acceptance, it is expected to increase gradually the number of ATCs. This should allow one to enhance the aforementioned values up to 11-17% photopeak efficiency, 6-11 keV FWHM energy resolution and ~40% P/T-ratio. The chosen γ-ray energy of $E_{\gamma,o} = 1$ MeV corresponds only to an average representative value, which is close to many experiments of interest for nuclear structure. Values for another γ-ray energies are reported below in Sec. 5.

5. Dependence of the performance on the γ-ray energy

The complex dependency of the detection efficiency on the γ-ray transition energy using relativistic RIBs can be best studied by means of MC simulations. On one hand, the Lorentz boost concentrates a large amount of γ-quanta in the forward direction, thus enhancing the detection probability for small values of the angle θ_γ, mostly in the region covered by the double cluster detectors. But on the other hand, this effect is counterbalanced to some extent by the Doppler shift in energy, which increases the γ-ray enery at forward angles, thus reducing the detection efficiency correspondingly. In order to quantify the impact of these effects in the performance of the tracking array, MC simulated values for efficiency, resolution and P/T-ratio, are tabulated and displayed in the following sections for

a range of γ-ray energies from 500 kev up to 5 MeV. Results are reported for three reference hybrid-shell AGATA geometries, namely 5.1) 10 triple- and 5 double-, 5.2) 5 triple- and 5 double- and 5.3) only 5-double cluster detectors.

5.1. 10 triple + 5 double cluster detectors

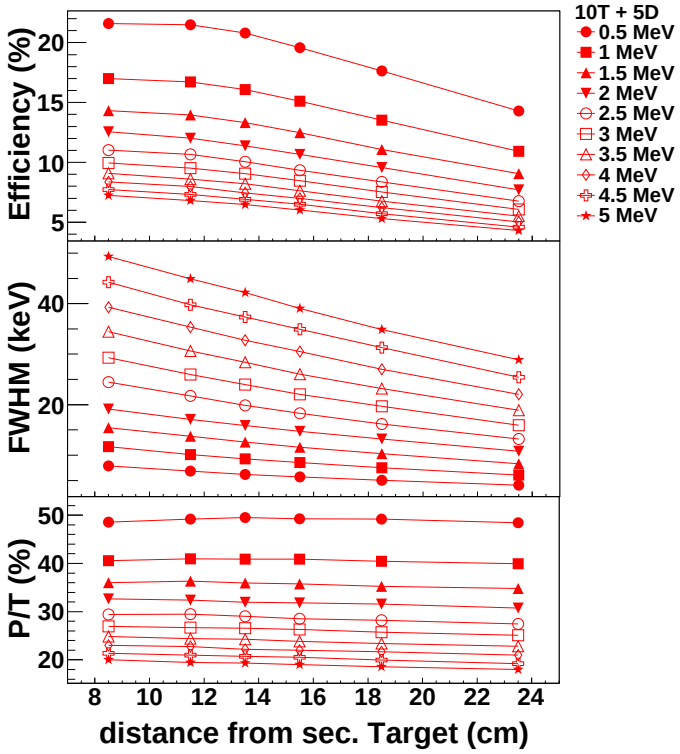

Figure 7: Photopeak efficiency (top), resolution (middle) and P/T ratio (bottom) for 10 triple + 5 double AGATA cluster detectors. Each curve corresponds to one γ-ray energy (see label). In all cases $\beta = 0.43$.

Table 2: 10 triple + 5 double AGATA configuration, efficiency and energy resolution values as a function of the γ-ray energy at rest $E_{\gamma,\circ}$ and $\beta = 0.43$.

$E_{\gamma,\circ}$	distance target-array (cm)						
(MeV)	23.5	18.5	15.5	13.5	11.5	8.5	
0.5 MeV	14.3	17.6	19.6	20.8	21.5	21.6	ε_γ (%)
	4.1	5.0	5.7	6.2	6.9	7.9	FWHM (keV)
	48.4	49.2	49.2	49.5	49.2	48.6	P/T (%)
1 MeV	10.9	13.5	15.1	16.1	16.7	17.0	ε_γ (%)
	6.1	7.5	8.5	9.3	10.1	11.7	FWHM (keV)
	39.9	40.5	40.9	40.9	41.0	40.6	P/T (%)
1.5 MeV	9.1	11.1	12.5	13.3	14.0	14.3	ε_γ (%)
	8.3	10.3	11.6	12.6	13.8	15.4	FWHM (keV)
	34.8	35.2	35.7	35.9	36.3	36.0	P/T (%)
2 MeV	7.7	9.6	10.7	11.4	12.0	12.6	ε_γ (%)
	10.8	13.2	14.7	15.9	17.1	19.1	FWHM (keV)
	30.8	31.5	31.8	31.9	32.4	32.6	P/T (%)
2.5 MeV	6.8	8.4	9.3	10.1	10.7	11.0	ε_γ (%)
	13.2	16.2	18.3	19.9	21.7	24.5	FWHM (keV)
	27.4	28.2	28.5	29.0	29.5	29.4	P/T (%)
3 MeV	6.1	7.5	8.5	9.1	9.5	9.9	ε_γ (%)
	15.9	19.7	22.0	24.0	26.0	29.3	FWHM (keV)
	25.1	25.7	26.3	26.6	26.7	26.9	P/T (%)
3.5 MeV	5.5	6.8	7.6	8.2	8.6	9.1	ε_γ (%)
	18.9	23.2	26.0	28.4	30.6	34.4	FWHM (keV)
	22.8	23.4	23.9	24.3	24.4	24.8	P/T (%)
4 MeV	5.0	6.2	7.0	7.5	8.0	8.4	ε_γ (%)
	22.0	27.0	30.5	32.8	35.3	39.3	FWHM (keV)
	21.0	21.7	22.0	22.2	22.8	23.0	P/T (%)
4.5 MeV	4.6	5.7	6.5	6.9	7.3	7.7	ε_γ (%)
	25.4	31.3	34.9	37.3	39.8	44.2	FWHM (keV)
	19.2	20.0	20.5	20.7	21.0	21.4	P/T (%)
5 MeV	4.3	5.3	6.0	6.5	6.8	7.2	ε_γ (%)
	28.9	34.9	39.0	42.2	44.9	49.3	FWHM (keV)
	18.0	18.6	19.0	19.3	19.5	20.0	P/T (%)

5.2. 7 triple + 5 double cluster detectors

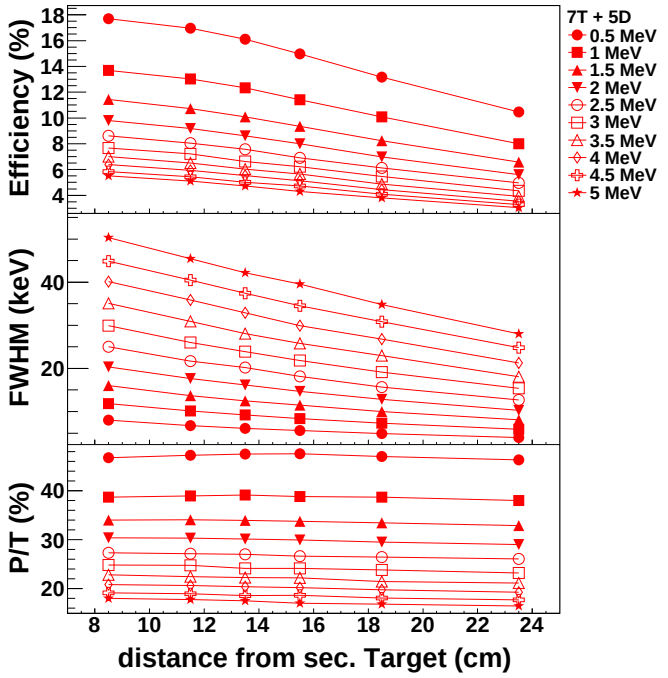

Figure 8: Photopeak efficiency (top), resolution (middle) and P/T ratio (bottom) for 7 triple + 5 double AGATA cluster detectors. Each curve corresponds to one γ-ray energy (see figure label). In all cases $\beta = 0.43$.

5.3. 5 triple + 5 double cluster detectors

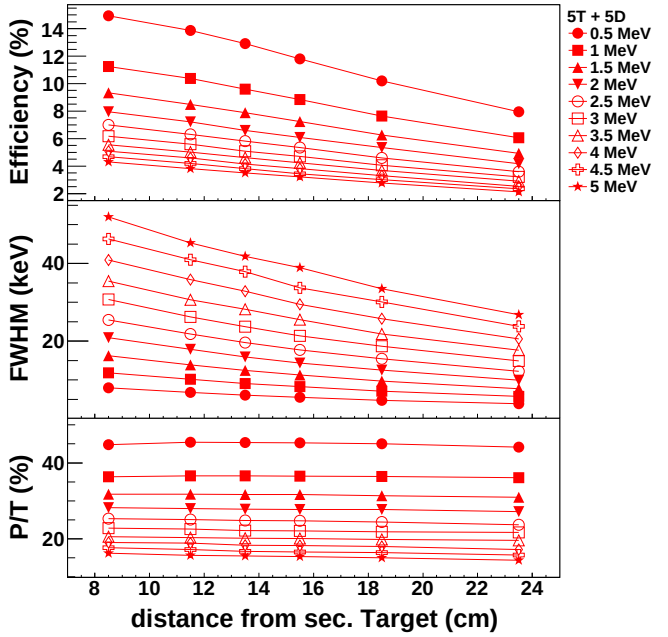

Figure 9: Photopeak efficiency (top), resolution (middle) and P/T ratio (bottom) for 5 triple + 5 double AGATA cluster detectors. Each curve corresponds to one γ-ray energy (see figure label). In all cases $\beta = 0.43$.

Table 3: 7 triple + 5 double AGATA configuration, efficiency, energy resolution and P/T-ratio values as a function of the γ-ray energy at rest $E_{\gamma,\circ}$ and $\beta = 0.43$.

$E_{\gamma,\circ}$ (MeV)	distance target-array (cm) 23.5	18.5	15.5	13.5	11.5	8.5	
0.5 MeV	10.5	13.2	15.0	16.1	17.0	17.7	ε_γ (%)
	3.9	4.9	5.6	6.1	6.8	8.0	FWHM (keV)
	46.3	47.0	47.6	47.5	47.2	46.7	P/T (%)
1 MeV	8.0	10.1	11.4	12.3	13.0	13.7	ε_γ (%)
	5.9	7.3	8.4	9.2	10.1	11.8	FWHM (keV)
	38.0	38.7	38.8	39.1	38.9	38.7	P/T (%)
1.5 MeV	6.6	8.2	9.4	10.1	10.7	11.4	ε_γ (%)
	8.1	10.0	11.5	12.5	13.7	16.0	FWHM (keV)
	32.9	33.4	33.8	33.9	34.0	34.0	P/T (%)
2 MeV	5.6	7.0	8.0	8.6	9.2	9.8	ε_γ (%)
	10.3	12.8	14.7	16.1	17.7	20.3	FWHM (keV)
	29.0	29.5	29.9	30.1	30.3	30.4	P/T (%)
2.5 MeV	5.0	6.1	6.9	7.6	8.0	8.6	ε_γ (%)
	12.7	15.7	18.2	20.2	21.7	25.0	FWHM (keV)
	26.1	26.5	26.6	27.0	27.1	27.3	P/T (%)
3 MeV	4.3	5.4	6.2	6.6	7.2	7.7	ε_γ (%)
	15.4	19.2	21.9	23.9	26.0	30.0	FWHM (keV)
	23.2	23.8	24.2	24.1	24.8	24.8	P/T (%)
3.5 MeV	3.9	4.9	5.7	6.0	6.5	7.0	ε_γ (%)
	18.1	22.9	25.8	28.1	30.9	35.1	FWHM (keV)
	21.2	21.5	22.2	22.3	22.5	22.8	P/T (%)
4 MeV	3.5	4.4	5.1	5.5	5.9	6.4	ε_γ (%)
	21.3	26.8	29.9	32.9	35.9	40.1	FWHM (keV)
	19.2	19.8	20.2	20.4	20.7	20.9	P/T (%)
4.5 MeV	3.3	4.1	4.7	5.0	5.4	5.8	ε_γ (%)
	24.8	30.8	34.6	37.4	40.5	44.9	FWHM (keV)
	17.7	18.1	18.6	18.6	19.0	19.2	P/T (%)
5 MeV	3.0	3.8	4.3	4.7	5.1	5.5	ε_γ (%)
	28.0	34.8	39.5	42.2	45.4	50.3	FWHM (keV)
	16.4	16.8	17.0	17.5	17.8	18.0	P/T (%)

Table 4: 5 triple + 5 double AGATA configuration, efficiency and resolution values as a function of the γ-ray energy at rest $E_{\gamma,\circ}$ and $\beta = 0.43$.

$E_{\gamma,\circ}$ (MeV)	distance target-array (cm) 23.5	18.5	15.5	13.5	11.5	8.5	
0.5 MeV	8.0	10.2	11.8	12.9	13.9	14.9	ε_γ (%)
	3.8	4.7	5.5	6.0	6.8	8.0	FWHM (keV)
	44.1	45.0	45.2	45.4	45.4	44.8	P/T (%)
1 MeV	6.1	7.6	8.8	9.6	10.4	11.2	ε_γ (%)
	5.7	7.1	8.2	9.1	10.2	11.8	FWHM (keV)
	36.1	36.4	36.5	36.6	36.6	36.4	P/T (%)
1.5 MeV	4.9	6.3	7.2	7.9	8.5	9.3	ε_γ (%)
	7.7	9.7	11.3	12.4	13.8	16.2	FWHM (keV)
	30.9	31.4	31.7	31.7	31.7	31.8	P/T (%)
2 MeV	4.2	5.4	6.1	6.6	7.2	8.0	ε_γ (%)
	9.9	12.5	14.3	15.9	17.9	20.8	FWHM (keV)
	27.2	27.8	27.7	27.8	28.0	28.2	P/T (%)
2.5 MeV	3.6	4.6	5.4	5.8	6.3	7.0	ε_γ (%)
	12.2	15.4	17.7	19.6	21.8	25.4	FWHM (keV)
	23.7	24.4	24.8	24.8	25.0	25.3	P/T (%)
3 MeV	3.2	4.1	4.7	5.1	5.6	6.2	ε_γ (%)
	14.9	18.7	21.4	23.7	26.2	30.7	FWHM (keV)
	21.7	21.8	22.1	22.1	22.6	22.8	P/T (%)
3.5 MeV	2.9	3.7	4.2	4.6	5.0	5.6	ε_γ (%)
	17.7	21.8	25.5	28.2	30.6	35.5	FWHM (keV)
	19.6	19.8	20.1	20.2	20.3	20.6	P/T (%)
4 MeV	2.5	3.3	3.8	4.2	4.6	5.1	ε_γ (%)
	20.5	25.8	29.4	32.9	35.9	40.9	FWHM (keV)
	17.2	18.0	18.2	18.3	18.8	19.0	P/T (%)
4.5 MeV	2.3	3.0	3.5	3.8	4.2	4.7	ε_γ (%)
	23.8	30.1	33.7	37.9	41.0	46.3	FWHM (keV)
	15.7	16.4	16.5	16.7	17.2	17.6	P/T (%)
5 MeV	2.1	2.8	3.2	3.5	3.8	4.3	ε_γ (%)
	26.8	33.5	38.9	41.8	45.3	51.9	FWHM (keV)
	14.4	15.0	15.3	15.5	15.7	16.2	P/T (%)

6. Angular distribution of the efficiency

Angular distribution measurements of γ-rays emitted by oriented nuclei have been a fundamental tool to investigate their multipolarity and electromagnetic character (see e.g. Ref. [47]). In addition, the angular distribution of the prompt γ-rays emitted after Coulomb excitation allows one to distinguish between the electromagnetic and the nuclear contributions to the excited states. Such studies were performed in the past using an array of EUROBALL cluster detectors [48, 41]. The high granularity of AGATA in conjunction with the large angular range represent a substantial advantage in order to study angular distributions in detail. The broad angular coverage arises not only from the number of germanium crystals available, but also from the possibility to shift the secondary target up- and downstream by ±15 cm. This is illustrated in Figure 10, where the γ-ray efficiency for $E_{\gamma,\circ} = 1$ MeV emitted from a nucleus at $\beta = 0.43$ is displayed as a function of the angle θ_γ in intervals of $\Delta\theta_\gamma = \pm 5°$.

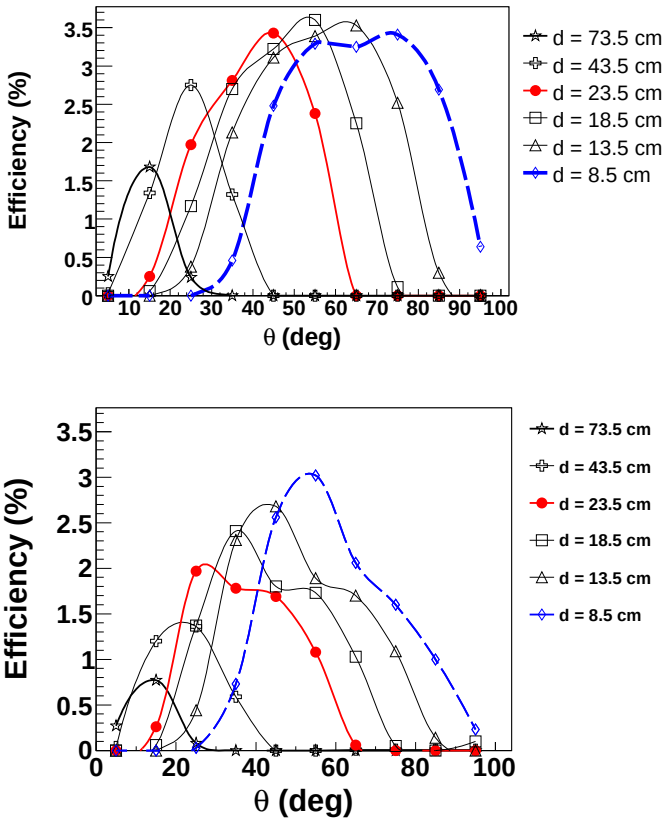

Figure 10: Efficiency as a function of the γ-ray detection angle θ_γ for $E_{\gamma,\circ} = 1$ MeV emitted at $\beta = 0.43$. (Top) A simulation with 10 triple and 5 double AGATA cluster detectors, (bottom) 5 triple and 5 double clusters.

Thus, in the AGATA configuration of 10 triple and 5 double cluster detectors, angles between 15° and 90° can be covered with angular efficiencies larger than 1%/10°. Note that at relativistic beam energies ($\beta \sim 0.43$), the largest differences between the electromagnetic and the nuclear interactions are obtained at $\theta_\gamma \simeq 25°$ and at $\theta_\gamma \simeq 60°$. At these angles, the pro-

posed geometry allows one to achieve efficiencies of more than 2.5% over an interval of $\Delta\theta_\gamma = \pm 5°$.

The angular distribution of the efficiency reflects the contribution of both, the inner ring of double-cluster and the outer ring of triple-cluster detectors. These two contributions are most visible in the "short" distance configuration (d=8.5 cm), where two maxima can be observed at ~55° and at ~75° (see Fig.10 top). Comparing the angular distribution of 10 T+5 D (Fig. 10 top) against that of 5 T+5 D (Fig. 10 bottom), one can indeed observe a reduction in the efficiency due to the lowering of the second maximum, i.e. the contribution of the outer ring of only five triple cluster detectors.

7. Impact of passive materials

At the final stage of the GSI-FRS the main source of γ-ray background is due to the slowing-down of ions and light-charged particles, which fly through layers of materials such as the energy-degrader, the secondary target, the tracking detectors and other structural materials like the beam-pipe and holding structures. Experimental γ-ray spectra with such a background are shown in previous publications [41, 49]. A description of this background at the lower beam-energies used in decay-spectroscopy experiments is reported in Ref. [50]. In order to suppress effectively this contaminant bremsstrahlung's radiation a lead layer of 2 mm thickness was installed around the EUROBALL cluster detectors in the past campaigns. In a similar way, it might be convenient to put a lead shielding around the reaction chamber to reduce the background in AGATA. This is a possibility which will be investigated during the commissioning of AGATA at GSI. The effect of such a lead layer with different thicknesses around the target chamber to shield the AGATA detectors is illustrated in Fig. 11, which shows the result of a MC simulation for $E_{\gamma,\circ} = 1$ MeV emitted at $\beta = 0.43$. Three configurations have been considered in the simulation, *i*) 10 triple + 5 double, *ii*) 5 triple + 5 double and *iii*) 5 double cluster detectors. The latter configuration (only 5 ADCs), as well as the shielding of 4 mm thickness are not realistic options, but they become useful to understand the trend and the systematic effect of passive materials placed between target and detectors. Indeed, the impact of a lead layer, both in the efficiency and in the P/T ratio, becomes larger for the ATCs than for the ADCs, and also for the short target-array distance of 8.5 cm than for the nominal distance (see Fig. 11). This reflects the energy shift due to the large Doppler effect at relativistic velocities, which yields smaller energies (larger absorption) at the larger angles subtended by the ATCs, when compared to the small angles (larger energy) subtended by the ADCs. The resolution (not shown in Fig. 11) remains practically unaffected.

8. Interplay between target thickness and halflife of the nuclear transition

The impact of the target characteristics and the excited state lifetime on the shape of Doppler corrected γ-ray spectra has

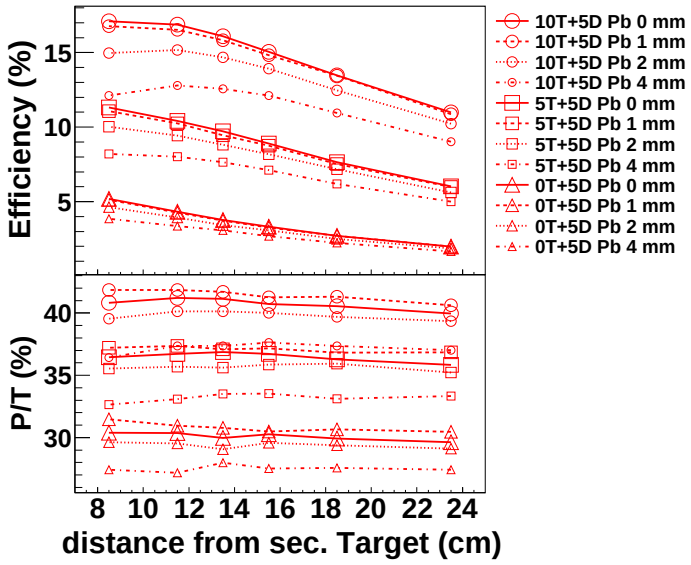

Figure 11: Biggest symbols represent values without lead absorber, the empty symbols with decreasing size show the deterioration of the efficiency (top panel) and P/T ratio (bottom) due to a layer of lead in-front of the detectors. See legend for proper interpretation of the absorber thickness. MC simulation performed for $E_{\gamma,\circ} = 1$ MeV emitted at $\beta = 0.43$.

been thoroughly investigated in Ref. [51] for in-beam γ-ray experiments at relativistic energies using the RISING array. A similar study for AGATA is presented in this section.

The convoluted effect of the excited state lifetime and the energy loss across the target thickness is due to the fact that the target is a passive element and therefore, both the ejectile velocity and position at de-excitation time, in general, remain unknown. In practice, only the measurement of the ejectile velocity after the target, β_{at}, becomes feasible. If the lifetime is sufficiently short, so that the average deexcitation path is shorter than the target thickness, most of the transitions still occur inside the target, where no kinematics information is available, i.e. the velocity at de-excitation time β is different, larger, than the velocity measured after the target β_{at} with LYCCA (see Sec. 2). On the other hand, nuclei with relatively long halflifes de-excite predominantly beyond the secondary target, and the velocity at deexcitation time β coincides with the velocity measured after the target β_{at}. In the latter case the Doppler correction becomes precise in terms of velocity. However, the deexcitation position downstream along the beam axis z remains still unknown and the true γ-ray emission angle θ_γ is larger than the one commonly assumed, which corresponds to deexcitations at the center of the target. This feature introduces an exponential tail towards low energy in the Doppler corrected photopeak, which is larger the longer is the lifetime. In general, the shape of the Doppler reconstructed spectrum reflects the contribution of these two effects, whose relative influence depends sensitively on the beam and target characteristics, as well as on the precise value of the transition lifetime. In order to illustrate this, a series of MC simulations have been carried out, with AGATA consisting of 10 ATC and 5 ADC, secondary targets of Au and

Be, with thicknesses of 250 and 500 mg/cm^2 and target-array distances of 8.5 and 23.5 cm. These are the most representative scenarios in terms of optimizing detection efficiency, resolution or reaction yield (see Sec. 2 and Sec. 3). For each case, transition halflifes between 0 ps and 100 ps have been simulated.

The physics case corresponds to a medium-heavy nucleus (Z=29, A=75) impinging at a velocity of $\beta = 0.43$ in the secondary target, and undergoing a one-proton knockout reaction. The spatial distribution along the beam direction z assumed for the generation of the primary events in the simulation corresponds to a constant excitation cross section across the path of the nucleus through the target. The event generator is the one described in Ref. [51] with only minor updates to interface with the standard AGATA-code [15]. A transition energy of $E_{\gamma,o} = 1$ MeV is assumed in all cases.

8.1. Light secondary target

The Doppler corrected spectra for beryllium targets of 250 and 500 mg/cm^2 are shown in Fig. 12 and Fig. 13, respectively. Also the spectrum corresponding to an ideally thin target is shown in those figures for comparison.

For the Doppler correction the (measurable) ejectile velocity after the target, β_{at}, has been considered and the γ-ray emission angle in the laboratory system, θ_γ, has been calculated assuming a deexcitation position along the beam axis at $z = 0$ cm, i.e., at the center of the target. The width of the photopeak reconstructed via MGT is reported in table 5. Note that in some cases the shape of the reconstructed photo-peak is rather asymmetric, and in those situations the value of the FWHM is not very representative.

Table 5: Energy resolution for a beryllium target and for several assumptions on the thickness and the halflife of the transition.

	RESOLUTION FWHM (keV)			
$t_{1/2}$	250 mg/cm^2		500 mg/cm^2	
(ps)	d=23.5 cm	d=8.5 cm	d=23.5 cm	d=8.5 cm
0	16.8	18.6	33.1	~32
1	15.9	16.7	35.5	27.2
10	11.2	16.9	9.2	16.5
50	16.8	~35	14.8	19.5
100	~30	~50	18.2	~30

As it was mentioned before, the main deviations from the ideal target case arise from two experimental effects. On one hand, for transitions where $t_{1/2}$ is small the width of the reconstructed peak is dominated by energy loss effects inside the target and the corresponding uncertainty on β at deexcitation time. As shown in the top panel of Fig.13, this effect is particularly prominent for the 500 mg/cm^2 target and for halflifes $t_{1/2} \lesssim 1$ ps. The tail towards high γ-ray energy is due to the assumption $\beta \sim \beta_{at}$. Actually, the fact that $\beta > \beta_{at}$ introduces a shift in the value of the Doppler reconstructed energy towards high energy (see Eq. 1). On the other hand, for transitions with large halflifes ($t_{1/2} \gtrsim 50$ ps) the width of the reconstructed peak is dominated by the uncertainty on the deexcitation position z

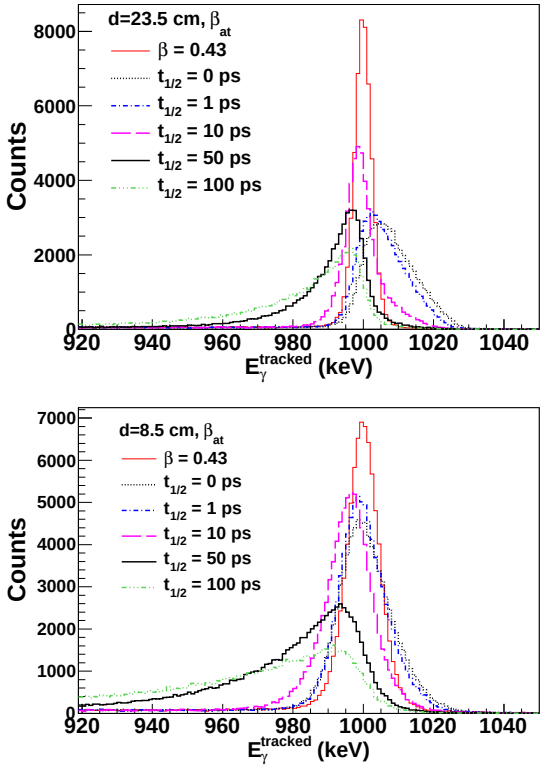

Figure 12: Effect of the lifetime and the energy loss across a 250 mg/cm^2 thick beryllium target. The velocity after the target has been taken for the Doppler reconstruction. Simulation for target-array distance of 23.5 cm (top) and 8.5 cm (bottom). The thin-solid line (labeled as $\beta = 0.43$) corresponds to an ideal target of negligible thickness and prompt deexcitations ($t_{1/2} = 0$ ps). See text for details.

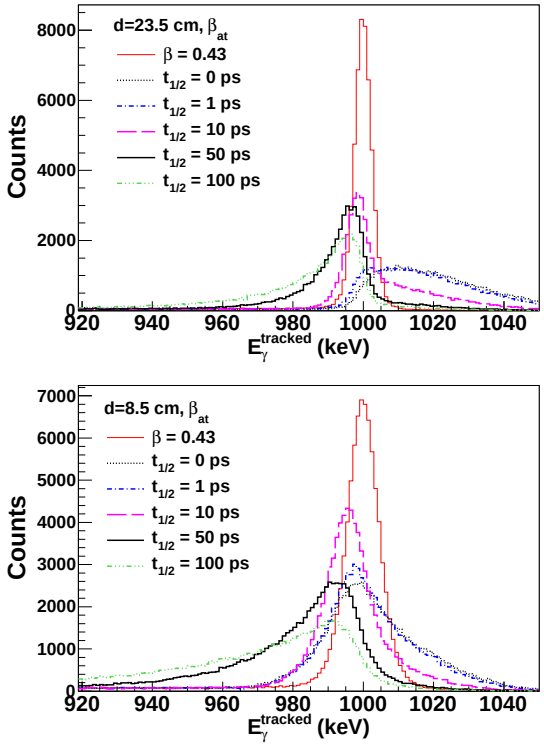

Figure 13: Same as Fig.12, but for a 500 mg/cm^2 thick Be-target.

along the beam axis. Assuming a deexcitation at $z = 0$ leads to an emission angle θ_γ smaller than the true angle downstream $z > 0$, an effect which goes in the opposite direction than the aforementioned $\beta \sim \beta_{at}$ approximation, shifting the value of the reconstructed energy towards low energy.

A remarkable improvement in the width of the reconstructed photopeak can be obtained if the value of the transition halflife is known, particularly for transitions with short lifetimes. Indeed, in these cases one can calculate the mean value for both, the ejectile velocity and the z-position at deexcitation time, and use them for the Doppler correction. In order to illustrate this we choose the example of the 500 mg/cm^2 Be-target at 8.5 cm (see Fig. 13-bottom). Table 6 shows the mean values of β and z at deexcitation time obtained from the MC-simulation.

Table 6: Mean β and z values at deexcitation time for the 500 mg/cm^2 thick Be-target.

τ (ps)	$<\beta>$	$<z>$ (mm)
0	0.401	0.0
1	0.397	0.2
10	0.380	1.8
50	0.371	8.8
100	0.369	17.5

As shown in Fig. 14, when instead of β_{at} and $z = 0$, the mean values of table 6 are used for the Doppler correction, one obtains rather symmetric distributions (at least for $t_{1/2} < 50$ ps), as well as an improvement in the width of the Doppler corrected photopeak ($\lesssim$20 keV FWHM for all transitions with $t_{1/2} < 50$ ps). On the other hand, when the value of the halflife is unknown, one can apply a multiple Doppler correction, assuming different values for the lifetime, and implementing in each case the corresponding mean position and velocity values. This might lead to an improved Doppler corrected spectrum, as well as to an estimate of the transition lifetime. More precise methods for the measurement of the lifetime are reported in Sec. 9.

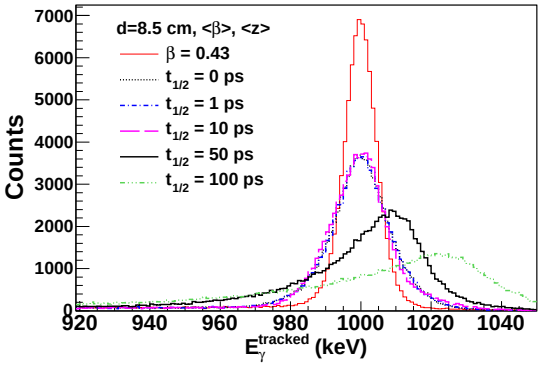

Figure 14: Same as Fig. 13-bottom, but assuming that the transition halflife is known, which allows one to use the mean velocity $<\beta>$ and the mean position $<z>$ values at deexcitation time for the Doppler correction of the spectrum.

8.2. *Heavy secondary target*

For secondary samples made of gold, the intrinsic stopping power is higher than for beryllium, but the distance which the ejectile needs to travel in order to cross the sample is a factor of 10 smaller. For gold targets one obtains the spectra shown in Fig. 15 and in Fig.16, for thicknesses of 250 mg/cm^2 and 500 mg/cm^2, respectively. The values for the energy resolution are listed in Table 7. For halflifes between 1 ps and 10 ps, for both target thicknesses most of the decays happen already after the target, thus yielding in both cases a rather thin distribution, which is only 1-4 keV broader than the ideally thin target case. This applies for both distances target-array of 23.5 cm and 8.5 cm. For shorter ($t_{1/2} < 1$ ps) or larger ($t_{1/2} > 10$ ps) halflifes, the width of the reconstructed peak increases by a factor of two, or more, owing to the aforementioned effects of larger uncertainties on β and on z-position at deexcitation time, respectively.

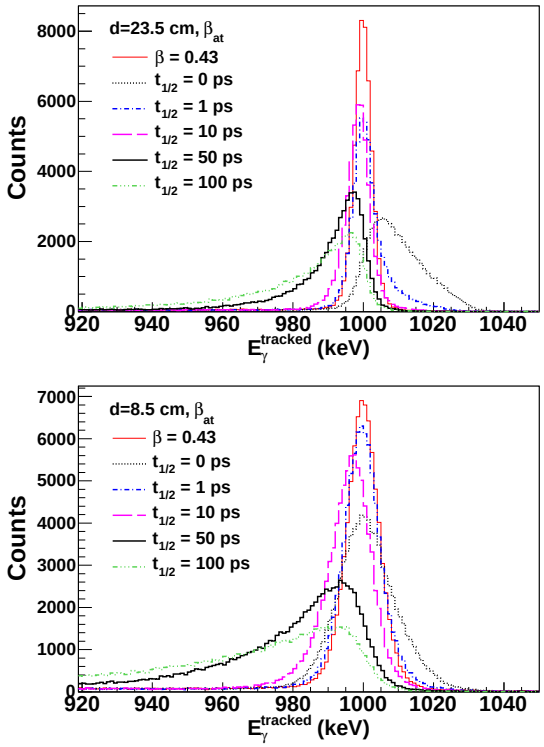

Figure 15: Same as Fig. 12, but for a gold target with a thickness of 250 mg/cm^2.

In summary, the attainable resolution at 1 MeV ranges between 7 keV and $\gtrsim$20 keV. The precise value depends sensitively on the projectile kinematics and characteristics (its atomic and mass numbers), target thickness and material, the target-array distance and the lifetime of the expected nuclear transition. In this respect, for the successful plan of in-flight experiments at GSI-FRS, it becomes convenient to perform in advance dedicated MC simulations, which include all these ingredients in a realistic way. This should allow one to optimize the experimental setup, and also select the secondary ion beam and the kinematics, which are best suited for the aim of each particular measurement.

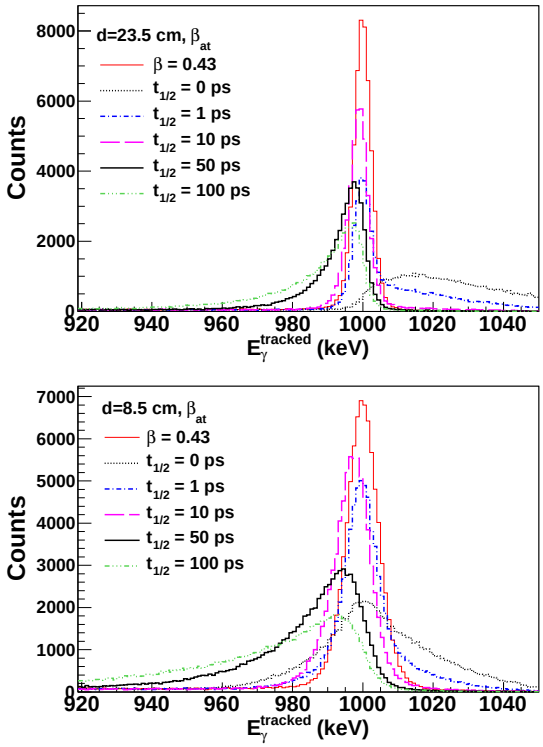

Figure 16: Same as Fig. 15, but for a gold target with a thickness of 500 mg/cm^2.

Table 7: Energy resolution for a gold target and for several assumptions on the thickness and the halflife of the transition.

	RESOLUTION FWHM (keV)			
$t_{1/2}$	250 mg/cm^2		500 mg/cm^2	
(ps)	d=23.5 cm	d=8.5 cm	d=23.5 cm	d=8.5 cm
0	16.4	19.9	~39	~34
1	8.9	13.4	6.9	15.3
10	8.4	15.2	7.1	13.4
50	14.4	14.4	11.7	18.2
100	~28	~33	12.5	26.5

9. Lifetime measurement

As described in Ref. [51], there are essentially two effects that can be exploited in order to evaluate the effective transition lifetime from the shape of the corresponding peak. The first one makes use of the dependence of the emission point along the beam axis z with the transition halflife. The second one uses the emission during the slow-down process. In this case the asymmetry of the reconstructed peak is larger at small angles.

The high position resolution, together with the possibility to work at target-array distance of 8.5 to 23.5 cm, makes AGATA particularly well suited for both methods.

9.1. Large lifetimes via centroid-shift at large angles

As described above in Sec. 8, this effect arises from the dependence of the average reaction-deexcitation distance on the value of the lifetime. Whereas for short lifetimes ($t_{1/2} \lesssim 1$ ps) the excited nucleus deexcites inside the target and, in good approximation, the mean de-exciation position along the beam axis corresponds to $z \sim 0$, for large lifetimes (~100 ps) this value is shifted towards higher distances z ~cm, thus being the real emission angle larger than the one obtained from the $z = 0$ assumption used for the Doppler reconstruction, and shifting the centroid of the γ-ray peak towards lower energy. Since the velocity of the products at $\beta \sim 0.4$ is of the order of 0.1-0.2 mm/ps, this effect is more evident for lifetime values of few tens to hundreds of ps. The best angular range to exploit this effect corresponds to angles, such that $\cos(\theta_\gamma) = \beta$ [51]. Thus, for the typical relativistic beam velocities of GSI-FRS $\beta = 0.43$, $\theta_\gamma \sim 65^\circ$ and, as shown in Fig. 10, the optimal AGATA configurations for covering such angles are those for target-array distances of 8.5 cm to 13.5 cm. The peak centroid-shift effects e.g. for a 250 mg/cm^2 Be target at 8.5 cm become evident in the spectra shown in the bottom panel of Fig. 12. The systematics of this shift with the halflife are displayed in Fig. 17, which demonstrates that halflifes in the range of 10 ps to 100 ps can be inferred via this method.

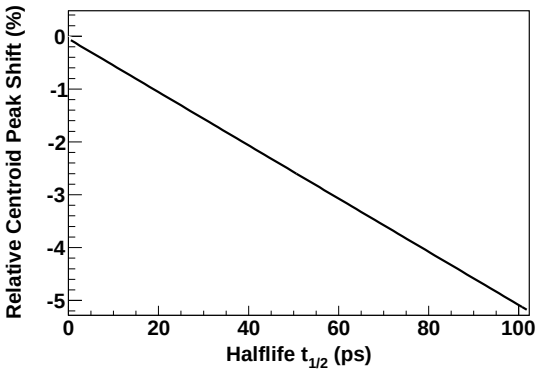

Figure 17: Systematics of the peak centroid shift for a 250 mg/cm^2 Be-target at 8.5 cm from the array (see text for details).

Because of the subtended angle and the range of halflifes, the shape of these spectra (Fig. 12-bottom) is dominated by the centroid-shift ($z > 0$) effects, although a small component towards high energy can be still appreciated for short halflifes

$t_{1/2} \lesssim 1$ ps. The high angular resolution of AGATA can be utilized here in order to disentangle the $z > 0$ effect of interest (which shifts the peak centroid towards lower values), from the effects of deexcitation during deceleration (which shift the distribution towards high energy). Thus, by applying an angular cut at $64° < \theta_\gamma < 66°$, one obtains the distributions shown in Fig. 18, which are fully dominated by the $z > 0$ effect.

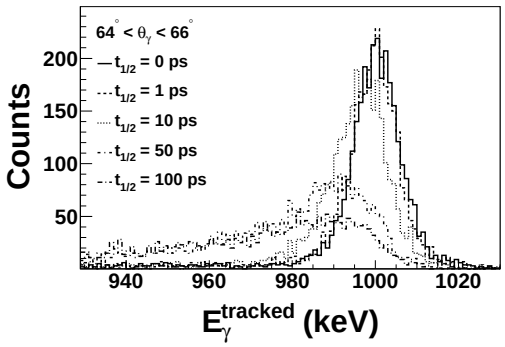

Figure 18: Line shape reconstructed for the 250 mg/cm^2 Be-target at 8.5 cm applying an angular cut of 65±1°.

9.2. *Small lifetimes via Doppler Shift Attenuation Method*

For lifetimes of few ps the Doppler-reconstructed photopeak typically shows two components. One of them is centered at the proper energy $E_{\gamma,\circ}$, and arises from deexcitations happening shortly after the target, where the velocity remains constant and can be measured. The second contribution extends towards $E_\gamma > E_{\gamma,\circ}$, and is due to deexcitations inside the target, where $\beta > \beta_{at}$. This tail towards high energy becomes more prominent at small angles (see Eq. 1). Indeed, at small angles θ_γ the shape of the Doppler corrected spectrum reflects the shape of the velocity distribution at deexcitation time. Fig. 19 shows quantitatively this effect for the example described in Sec. 8, now assuming halflife values between 0.25 ps and 1.5 ps, a gold target of 500 mg/cm^2 and a secondary beam energy of 150 MeV/u. Fig. 20 shows the Doppler reconstructed peak for several angular slices of $\Delta\theta_\gamma = 4°$ at forward angles of the $d = 23.5$ cm AGATA configuration, between 22° and 42°.

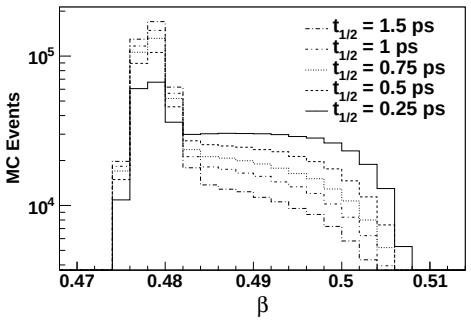

Figure 19: β-value at deexcitation time of the ejectile in a gold target 500 mg/cm^2 thick for an initial beam energy of 150 MeV/u.

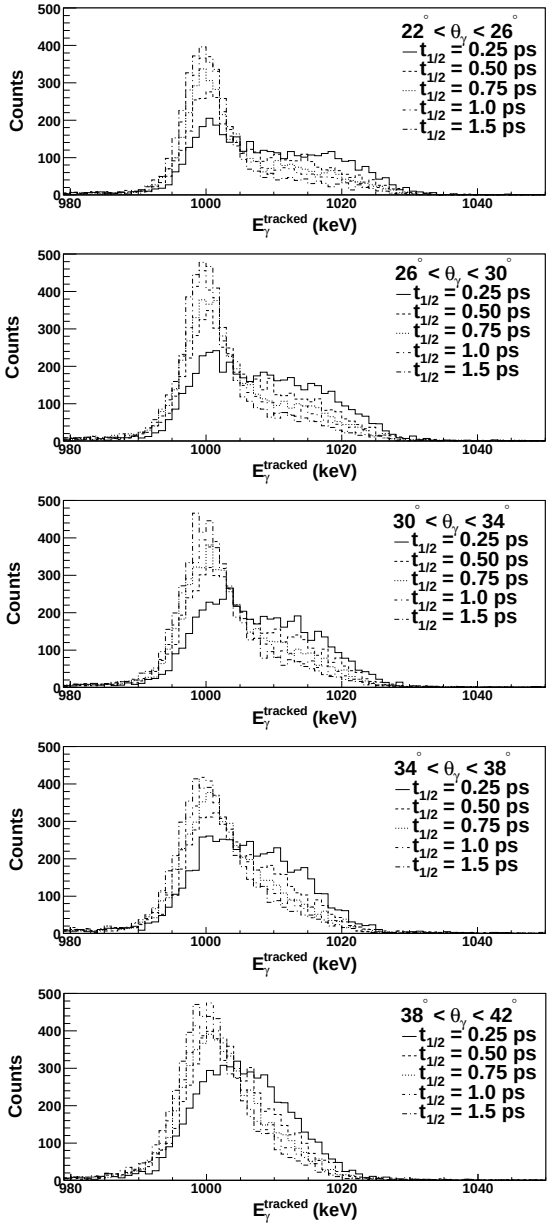

Figure 20: Doppler reconstructed spectra for several angular slices. Halflifes between 0.25 and 1.5 ps have been simulated. See text for details.

Thus, the fine angular resolution of AGATA allows one to measure accurately the angular evolution of the Doppler corrected photopeak. By comparing the systematics of this trend, versus detailed MC-simulations one can determine the value of rather fast nuclear transitions, approximately betten 200 fs and 2 ps.

10. Summary and conclusions

The R&D and the final conceptual design of AGATA for experiments at GSI-FRS has been presented. The solution proposed requires the development of AGATA double cluster detectors, thus aiming at a full optimization of the tracking array for in-beam γ-ray spectroscopy experiments at this facility. A systematic study based on Monte Carlo simulations is reported, which comprises several parameters such as the distance target-array, number of detectors available, energy of the γ-ray transition and influence of passive elements. Thus, for relativistic beams with $\beta = 0.43$, using an AGATA configuration of 5 double- and 5 triple-cluster detectors, photopeak efficiencies between 6% and 11% can be obtained for $E_{\gamma,\circ} = 1$ MeV (energy at rest), and target-array distances of 23.5 cm and 8.5 cm, respectively. These values become 11% and 17% respectively, when five additional triple cluster detectors would be available. The energy resolution attainable in Doppler corrected spectra depends on the particular experiment details and it seems to be, in most cases, dominated by energy loss effects in the secondary target and by the halflife of the expected transition. In this respect, it is recommended to carry out dedicated simulations in order to obtain realistic values for each particular experiment. As follow-up of a previous publication [51], the application of lineshape effects measurable with AGATA for the determination of transition halflifes has been investigated. Thus, using the AGATA response at large angles $\theta \sim 65°$, and at short angles $\theta \sim 20 - 30°$, our simulation shows that it is possible to determine the value of halflifes of 10-100 ps, and 0.1-1 ps, respectively.

Acknowledgement

The authors acknowledge support from HIC4FAIR. This work has been supported in part by MEC (Spain) under grants FPAXXX and FPAXXX.

References

[1] F. A. Beck. EUROBALL: Large gamma ray spectrometers through european collaborations. *Progress in Particle and Nuclear Physics*, 28:443–461, 1992.

[2] I. Y. Lee. The Gammasphere. *Nuclear Physics A*, 520:641–+, December 1990.

[3] R. M. Diamond, editor. *High-spin gamma-ray spectroscopy*, March 1984.

[4] P. J. Twin, P. J. Nolan, R. Aryaeinejad, D. J. G. Love, A. H. Nelson, and A. Kirwan. TESSA : A multi-detector γ-ray array designed to study high spin states. *Nuclear Physics A*, 409:343–351, November 1983.

[5] O. Moller, A. Dewald, P. Petkov, B. Saha, A. Fitzler, K. Jessen, D. Tonev, T. Klug, S. Heinze, J. Jolie, P. von Brentano, D. Bazzacco, C. A. Ur, E. Farnea, M. Axiotis, S. Lunardi, G. de Angelis, D. R. Napoli, N. Marginean, T. Martinez, M. A. Caprio, and R. F. Casten. Electromagnetic transition strengths in ^{156}dy. *Phys.Rev. C*, 74:024313, 2006.

[6] P. Petkov, A. Dewald, O. Moller, B. Saha, A. Fitzler, K. Jessen, D. Tonev, T. Klug, S. Heinze, J. Jolie, P. von Brentano, D. Bazzacco, C. Ur, E. Farnea, M. Axiotis, S. Lunardi, C. Rossi-Alvarez, G. de Angelis, D. R. Napoli, N. Marginean, T. Martinez, M. Caprio, and R. F. Casten. Collectivity at high spins in ^{156}dy. *Phys.Rev. C*, 68:034328, 2003.

[7] M. A. Caprio, N. V. Zamfir, R. F. Casten, C. J. Barton, C. W. Beausang, J. R. Cooper, A. A. Hecht, R. Krucken, H. Newman, J. R. Novak, N. Pietralla, A. Wolf, and K. E. Zyromski. Low-spin structure of ^{156}dy through γ-ray spectroscopy. *Phys.Rev. C*, 66:054310, 2002.

[8] P. J. Twin, B. M. Nyakó, A. H. Nelson, J. Simpson, M. A. Bentley, H. W. Cranmer-Gordon, P. D. Forsyth, D. Howe, A. R. Mokhtar, J. D. Morrison, J. F. Sharpey-Schafer, and G. Sletten. Observation of a discrete-line superdeformed band up to $60\hbar$ in ^{152}Dy. *Physical Review Letters*, 57:811–814, August 1986.

[9] Perspectives of Nuclear Physics in Europe, NuPECC Long Range Plan 2010, 2010. European Science Foundation.

[10] J. Gerl, W. Korten (Eds.), AGATA: Technical Proposal for an Advanced Gamma Tracking Array for the European Gamma Spectroscopy Community, (2001) <http://agata.pd.infn.it>.

[11] M. A. Deleplanque, I. Y. Lee, K. Vetter, G. J. Schmid, F. S. Stephens, R. M. Clark, R. M. Diamond, P. Fallon, and A. O. Macchiavelli. GRETA: utilizing new concepts in γ-ray detection. *Nuclear Instruments and Methods in Physics Research A*, 430:292–310, July 1999.

[12] F. Camera. AGATA: The European HPGe tracking array. In A. J. Kreiner & O. Civitarese, editor, *VI Latin American Symposium on Nuclear Physics and Applications*, volume 884 of *American Institute of Physics Conference Series*, pages 97–102, February 2007.

[13] E. Ince, E. Farnea, A. Latina, and M. N. Erduran. Realistic simulations of the AGATA Demonstrator+PRISMA Spectrometer. In I. Boztosun & A. B. Balantekin, editor, *American Institute of Physics Conference Series*, volume 1072 of *American Institute of Physics Conference Series*, pages 273–276, November 2008.

[14] E. Farnea. The AGATA Demonstrator Array at Laboratori Nazionali di Legnaro: Status of the Project. In M. Milin, T. Niksic, S. Szilner, & D. Vretenar, editor, *American Institute of Physics Conference Series*, volume 1165 of *American Institute of Physics Conference Series*, pages 390–393, August 2009.

[15] The Agata Collaboration, E. Farnea, F. Recchia, D. Bazzacco, T. Kröll, Z. Podolyák, B. Quintana, A. Gadea, and The AGATA Collaboration. Conceptual design and Monte Carlo simulations of the AGATA array. *Nuclear Instruments and Methods in Physics Research A*, 621:331–343, September 2010.

[16] The Agata, Prisma Collaborations, E. Ince, M. N. Erduran, E. Farnea, A. Latina, G. Pollarolo, and The AGATA and PRISMA Collaborations. Realistic simulations of the AGATA Demonstrator+PRISMA spectrometer. *Nuclear Instruments and Methods in Physics Research A*, 622:107–112, October 2010.

[17] A. Al-Adili. Simulations of Doppler Effects in Nuclear Reactions for AGATA Commissioning Experiments. *ArXiv e-prints*, September 2009.

[18] P. Reiter, B. Bruyneel, J. Eberth, H. Hess, G. Pascovici, N. Warr, A. Wiens, and H.-G. Thomas. The New Position Sensitive Triple Cluster Detector For AGATA. In J. Jolie, A. Zilges, N. Warr, & A. Blazhev, editor, *American Institute of Physics Conference Series*, volume 1090 of *American Institute of Physics Conference Series*, pages 97–101, January 2009.

[19] L. Nelson, M. R. Dimmock, A. J. Boston, H. C. Boston, J. R. Cresswell, P. J. Nolan, I. Lazarus, J. Simpson, P. Medina, C. Santos, and C. Parisel. Characterisation of an AGATA symmetric prototype detector. *Nuclear Instruments and Methods in Physics Research A*, 573:153–156, April 2007.

[20] H. C. Boston, J. R. Cresswell, M. R. Dimmock, L. Nelson, P. J. Nolan, S. Rigby, I. Lazarus, J. Simpson, P. Medina, C. Santos, C. Parisel, and The AGATA Collaboration. Gamma-ray tracking: Characterisation of the AGATA symmetric prototype detectors. *Nuclear Instruments and Methods in Physics Research B*, 261:1098–1102, August 2007.

[21] A. J. Boston, M. R. Dimmock, C. Unsworth, H. C. Boston, R. J. Cooper, A. N. Grint, L. J. Harkness, I. H. Lazarus, M. Jones, P. J. Nolan, D. C. Oxley, J. Simpson, and M. Slee. Performance of an AGATA asymmetric detector. In I. Boztosun & A. B. Balantekin, editor, *American Institute of Physics Conference Series*, volume 1072 of *American Institute of Physics Conference Series*, pages 130–135, November 2008.

[22] C. Unsworth, A. J. Boston, H. C. Boston, S. Colosimo, J. Cresswell, M. R.

Dimmock, F. Filmer, D. Judson, S. Moon, P. J. Nolan, M. J. Norman, and M. Slee. Characterisation of an asymmetric AGATA detector. In *Society of Photo-Optical Instrumentation Engineers (SPIE) Conference Series*, volume 7449 of *Society of Photo-Optical Instrumentation Engineers (SPIE) Conference Series*, August 2009.

[23] M. R. Dimmock, A. J. Boston, J. R. Cresswell, I. Lazarus, P. Medina, P. Nolan, C. Parisel, C. Santos, J. Simpson, and C. Unsworth. Validation of Pulse Shape Simulations for an AGATA Prototype Detector. *IEEE Transactions on Nuclear Science*, 56:2415–2425, August 2009.

[24] M. R. Dimmock, A. J. Boston, H. C. Boston, J. R. Cresswell, L. Nelson, P. J. Nolan, C. Unsworth, I. H. Lazarus, and J. Simpson. Characterisation Results From an AGATA Prototype Detector. *IEEE Transactions on Nuclear Science*, 56:1593–1599, June 2009.

[25] The Agata Collaboration, A. J. Boston, M. R. Dimmock, C. Unsworth, H. C. Boston, R. J. Cooper, A. N. Grint, L. J. Harkness, I. H. Lazarus, M. Jones, P. J. Nolan, D. C. Oxley, J. Simpson, M. Slee, and the AGATA Collaboration. Performance of an AGATA asymmetric detector. *Nuclear Instruments and Methods in Physics Research A*, 604:48–52, June 2009.

[26] A. J. Boston, M. R. Dimmock, C. Unsworth, H. C. Boston, R. J. Cooper, A. N. Grint, L. J. Harkness, I. H. Lazarus, M. Jones, P. J. Nolan, D. C. Oxley, J. Simpson, and M. Slee. Status and Performance of an AGATA asymmetric detector. In D. Dashdorj, U. Agvaanluvsan, & G. E. Mitchell, editor, *American Institute of Physics Conference Series*, volume 1109 of *American Institute of Physics Conference Series*, pages 38–43, March 2009.

[27] M. Bellato, L. Berti, D. Bortolato, P. J. Coleman-Smith, P. Edelbruck, X. Grave, R. Isocrate, I. Lazarus, D. Linget, P. Medina, C. Oziol, G. Rampazzo, C. Santos, B. Travers, and A. Triossi. Global Trigger and Readout System for the AGATA Experiment. *IEEE Transactions on Nuclear Science*, 55:91–98, 2008.

[28] F. Zocca, A. Pullia, D. Bazzacco, and G. Pascovici. A Time-Over-Threshold Technique for Wide Dynamic Range Gamma-Ray Spectroscopy With the AGATA Detector. *IEEE Transactions on Nuclear Science*, 56:2384–2391, August 2009.

[29] S. Akkoyun, A. Algora, B. Alikhani, F. Ameil, G. de Angelis, L. Arnold, A. Astier, A. Ataç, Y. Aubert, C. Aufranc, and et al. AGATA–Advanced GAmma Tracking Array. *Nuclear Instruments and Methods in Physics Research A*, 668:26–58, March 2012.

[30] F. Recchia, D. Bazzacco, E. Farnea, A. Gadea, R. Venturelli, T. Beck, P. Bednarczyk, A. Buerger, A. Dewald, M. Dimmock, G. Duchêne, J. Eberth, T. Faul, J. Gerl, R. Gernhaeuser, K. Hauschild, A. Holler, P. Jones, W. Korten, T. Kröll, R. Krücken, N. Kurz, J. Ljungvall, S. Lunardi, P. Maierbeck, D. Mengoni, J. Nyberg, L. Nelson, G. Pascovici, P. Reiter, H. Schaffner, M. Schlarb, T. Steinhardt, O. Thelen, C. A. Ur, J. J. Valiente Dobon, and D. Weißhaar. Position resolution of the prototype AGATA triple-cluster detector from an in-beam experiment. *Nuclear Instruments and Methods in Physics Research A*, 604:555–562, June 2009.

[31] For The Agata Collaboration, F. Recchia, D. Bazzacco, E. Farnea, R. Venturelli, S. Aydin, G. Suliman, C. A. Ur, and For the AGATA Collaboration. Performance of an AGATA prototype detector estimated by Compton-imaging techniques. *Nuclear Instruments and Methods in Physics Research A*, 604:60–63, June 2009.

[32] For The Agata Collaboration, A. Wiens, H. Hess, B. Birkenbach, B. Bruyneel, J. Eberth, D. Lersch, G. Pascovici, P. Reiter, H.-G. Thomas, and for the AGATA Collaboration. The AGATA triple cluster detector. *Nuclear Instruments and Methods in Physics Research A*, 618:223–233, June 2010.

[33] F. Recchia. Installation of the AGATA Demonstrator and commissioning experiments at LNL. *Journal of Physics Conference Series*, 205(1):012045–+, January 2010.

[34] F. Recchia. In-Beam Test of the AGATA Prototype Triple Cluster. *Acta Physica Polonica B*, 38:1297–+, April 2007.

[35] P. A. Söderström, A. Al-Adili, J. Nyberg, F. Recchia, E. Farnea, and A. Gadea. Gamma tracking with the AGATA detector. In *Proceedings of the 17th International Workshop on Vertex detectors. July 28-August 1, 2008. Utö Island, Sweden. Published online at ¡A href="http://pos.sissa.it/cgi-bin/reader/conf.cgi?confid=68"¿http://pos.sissa.it/cgi-bin/reader/conf.cgi?confid=68¡/A¿, p.40*, 2008.

[36] A. Ataç, A. Kaşkaş, S. Akkoyun, M. Şenyiğit, T. Hüyük, S. O. Kara, and J. Nyberg. Discrimination of gamma rays due to inelastic neutron scattering in AGATA. *Nuclear Instruments and Methods in Physics Research A*, 607:554–563, August 2009.

[37] The Agata Collaboration, M. Doncel, F. Recchia, B. Quintana, A. Gadea, E. Farnea, and The AGATA Collaboration. Experimental test of the background rejection, through imaging capability, of a highly segmented AGATA germanium detector. *Nuclear Instruments and Methods in Physics Research A*, 622:614–618, October 2010.

[38] M. Doncel, F. Recchia, A. Gadea, E. Farnea, and B. Quintana. Compton Imaging Capabilities of AGATA for Background Rejection. In J. A. Caballero, C. E. Alonso, M. V. Andrés, J. E. García Ramos, & F. Pérez-Bernal, editor, *American Institute of Physics Conference Series*, volume 1231 of *American Institute of Physics Conference Series*, pages 213–214, April 2010.

[39] J. Gerl. Nuclear Spectroscopy Studies at GSI – from Rising to HISPEC/DESPEC. *Acta Physica Polonica B*, 40:767–+, March 2009.

[40] M. Winkler, H. Geissel, H. Weick, B. Achenbach, K.-H. Behr, D. Boutin, A. Brünle, M. Gleim, W. Hüller, C. Karagiannis, A. Kelic, B. Kindler, E. Kozlova, H. Leibrock, B. Lommel, G. Moritz, C. Mühle, G. Münzenberg, C. Nociforo, W. Plass, C. Scheidenberger, H. Simon, K. Sümmerer, N. A. Tahir, A. Tauschwitz, M. Tomut, J. S. Winfield, and M. Yavor. The status of the Super-FRS in-flight facility at FAIR. *Nuclear Instruments and Methods in Physics Research B*, 266:4183–4187, October 2008.

[41] P. Bednarczyk, J. Grębosz, M. Kmiecik, A. Maj, W. Męczyński, J. Styczeń, C. Domingo-Pardo, P. Doornenbal, Gerl J., M. Górska, H. J. Wollersheim, J. Jolie, P. Reiter, A. Bracco, and F. Camera. In-beam γ-ray angular distribution and lifetime measurements - experience from rising and perspectives at FAIR. *Acta Physica Polonica B*, 41:505–+, January 2010.

[42] H. Geissel, P. Armbruster, K. H. Behr, A. Brünle, K. Burkard, M. Chen, H. Folger, B. Franczak, H. Keller, O. Klepper, B. Langenbeck, F. Nickel, E. Pfeng, M. Pfützner, E. Roeckl, K. Rykaczewski, I. Schall, D. Schardt, C. Scheidenberger, K.-H. Schmidt, A. Schröter, T. Schwab, K. Sümmerer, M. Weber, G. Münzenberg, T. Brohm, H.-G. Clerc, M. Fauerbach, J.-J. Gaimard, A. Grewe, E. Hanelt, B. Knödler, M. Steiner, B. Voss, J. Weckenmann, C. Ziegler, A. Magel, H. Wollnik, J. P. Dufour, Y. Fujita, D. J. Vieira, and B. Sherrill. The GSI projectile fragment separator (FRS): a versatile magnetic system for relativistic heavy ions. *Nuclear Instruments and Methods in Physics Research B*, 70:286–297, August 1992.

[43] D. Rudolph et al. LYCCA - the Lund York Cologne CAlorimeter. Technical report, FAIR TAC HISPEC/DESPEC, 2010.

[44] H. J. Wollersheim, D. E. Appelbe, A. Banu, R. Bassini, T. Beck, F. Becker, P. Bednarczyk, K.-H. Behr, M. A. Bentley, G. Benzoni, C. Boiano, U. Bonnes, A. Bracco, S. Brambilla, A. Brunle, A. Burger, K. Burkard, P. A. Butler, F. Camera, D. Curien, J. Devin, P. Doornenbal, C. Fahlander, K. Fayz, H. Geissel, J. Gerl, M. Gorska, H. Grawe, J. Grebosz, R. Griffiths, G. Hammond, M. Hellstrom, J. Hoffmann, H. Hubel, J. Jolie, J. V. Kalben, M. Kmiecik, I. Kojouharov, R. Kulessa, N. Kurz, I. Lazarus, J. Li, J. Leske, R. Lozeva, A. Maj, S. Mandal, W. Meczynski, B. Million, G. Munzenberg, S. Muralithar, M. Mutterer, P. J. Nolan, G. Neyens, J. Nyberg, W. Prokopowicz, V. F. E. Pucknell, P. Reiter, D. Rudolph, N. Saito, T. R. Saito, D. Seddon, H. Schaffner, J. Simpson, K.-H. Speidel, J. Styczen, K. Summerer, N. Warr, H. Weick, C. Wheldon, O. Wieland, M. Winkler, and M. Zieblinski. Rare ISotopes INvestigation at GSI (RISING) using gamma-ray spectroscopy at relativistic energies. *Nuclear Instruments and Methods in Physics Research A*, 537:637–657, February 2005.

[45] D. Bazzacco. mgt code developed within the tmr program 'gamma-ray tracking detectors'.

[46] C. Nochiforo, private communication.

[47] J. A. Grau, Z. W. Grabowski, F. A. Rickey, P. C. Simms, and R. M. Steffen. Measurements of Directional Correlation from Oriented Nuclei (DCO) and the Band Structure in ^{102}Pd. *Physical Review Letters*, 32:677–680, March 1974.

[48] P. Bednarczyk, J. Grębosz, A. Maj, M. Kmiecik, W. Męczyński, J. Styczeń, H. J. Wollersheim, J. Gerl, M. Górska, P. Reiter, A. Bracco, and F. Camera. Gamma-Ray Angular Distribution in Coulomb Excitation Experiments at Intermediate Energies as a Signature of Electromagnetic and Nuclear Forces in Peripheral Collisions. *Acta Physica Polonica B*, 40:853–+, March 2009.

[49] T. R. Saito, N. Saito, K. Starosta, J. Beller, N. Pietralla, H. J. Wollersheim,

D. L. Balabanski, A. Banu, R. A. Bark, T. Beck, F. Becker, P. Bednarczyk, K.-H. Behr, G. Benzoni, P. G. Bizzeti, C. Boiano, A. Bracco, S. Brambilla, A. Brünle, A. Bürger, L. Caceres, F. Camera, F. C. L. Crespi, P. Doornenbal, A. B. Garnsworthy, H. Geissel, J. Gerl, M. Górska, J. Grebosz, G. Hagemann, J. Jolie, M. Kavatsyuk, O. Kavatsyuk, T. Koike, I. Kojouharov, N. Kurz, J. Leske, G. Lo Bianco, A. Maj, S. Mallion, S. Mandal, M. Maliage, T. Otsuka, C. M. Petrache, Z. Podolyak, W. Prokopowicz, G. Rainovski, P. Reiter, A. Richard, H. Schaffner, S. Schielke, G. Sletten, N. J. Thompson, D. Tonev, J. Walker, N. Warr, O. Wieland, and Q. Zhong. Yrast and non-yrast 2^+ states of ^{134}Ce and ^{136}Nd populated in relativistic Coulomb excitation. *Physics Letters B*, 669:19–23, October 2008.

[50] P. Detistov, D. L. Balabanski, and Z. Podolyak. Simulation of the Electromagnetic Background Radiation for the Rising Experimental Set-Up. *Acta Physica Polonica B*, 38:1287–+, April 2007.

[51] P. Doornenbal, P. Reiter, H. Grawe, T. Saito, A. Al-Khatib, A. Banu, T. Beck, F. Becker, P. Bednarczyk, G. Benzoni, A. Bracco, A. Bürger, L. Caceres, F. Camera, S. Chmel, F. C. L. Crespi, H. Geissel, J. Gerl, M. Górska, J. Grębosz, H. Hübel, M. Kavatsyuk, O. Kavatsyuk, M. Kmiecik, I. Kojouharov, N. Kurz, R. Lozeva, A. Maj, S. Mandal, W. Meczynski, B. Million, Z. Podolyák, A. Richard, N. Saito, H. Schaffner, M. Seidlitz, T. Striepling, J. Walker, N. Warr, H. Weick, O. Wieland, M. Winkler, and H. J. Wollersheim. Lifetime effects for high-resolution gamma-ray spectroscopy at relativistic energies and their implications for the RISING spectrometer. *Nuclear Instruments and Methods in Physics Research A*, 613:218–225, February 2010.